Optics Communications 412 (2018) 201–213

Contents lists available at ScienceDirect

Optics Communications

journal homepage: www.elsevier.com/locate/optcom

Optical aberration correction for simple lenses via sparse representation

Jinlin Cui [a,b], Wei Huang [a,*]

[a] Changchun Institute of Optics, Fine Mechanics and Physics, Chinese Academy of Science, Changchun 130033, China
[b] University of Chinese Academy of Science, Beijing 100049, China

ARTICLE INFO

Keywords:
Image reconstruction resolution
Blind deconvolution
Nonblind deconvolution
Digital image processing
Lens system design

ABSTRACT

Simple lenses with spherical surfaces are lightweight, inexpensive, highly flexible, and can be easily processed. However, they suffer from optical aberrations that lead to limitations in high-quality photography. In this study, we propose a set of computational photography techniques based on sparse signal representation to remove optical aberrations, thereby allowing the recovery of images captured through a single-lens camera. The primary advantage of the proposed method is that many prior point spread functions calibrated at different depths are successfully used for restoring visual images in a short time, which can be generally applied to nonblind deconvolution methods for solving the problem of the excessive processing time caused by the number of point spread functions. The optical software CODE V is applied for examining the reliability of the proposed method by simulation. The simulation results reveal that the suggested method outperforms the traditional methods. Moreover, the performance of a single-lens camera is significantly enhanced both qualitatively and perceptually. Particularly, the prior information obtained by CODE V can be used for processing the real images of a single-lens camera, which provides an alternative approach to conveniently and accurately obtain point spread functions of single-lens cameras.

1. Introduction

Simple lenses with spherical surfaces are lightweight, inexpensive, easy to process, yet highly flexible optical equipment that can be used for numerous applications such as single-lens cameras. However, simple lenses with spherical surfaces suffer from optical aberrations that can seriously reduce image quality. Therefore, they cannot be directly used in high-resolution and high-quality photography. To enhance the performance of such imaging systems, different types of optical methods are used for optimization and compensating for aberrations such as increasing the number of lenses and using aspheric surfaces. Even though these methods significantly enhance the performance of optical imaging systems, they have high cost, structure complexity, volume, and weight problems.

Photography has attracted the attention of researchers who have been studying imaging sensors for a long time, not only to decrease the requirements of the hardware but also to enhance the performance of simple imaging systems. Recently, photography was transformed by computational photography that combines digital image processing with imaging systems for image restoration [1]. The basic methods of image restoration can be classified into two categories: blind deconvolution method [2–4] and nonblind deconvolution approach [5–8] depending on whether the point spread function (PSF) is known. Over the years, many deconvolution approaches have been developed, varying considerably in their speed and sophistication. Blind deconvolution algorithms can obtain superior images by employing the features of degraded images to estimate PSFs. However, the minimum of the resulting cost function does not correspond to a true sharp solution. This is particularly true if there is no evident enhancement in the degraded images when the optical aberrations are substantial. In contrast, nonblind deconvolution algorithms can significantly enhance the quality of images using the calibrated PSFs of imaging systems. These prior PSFs are typically measured at a single depth, thereby leading to inadequate results or even failures when the objects are outside the calibration plane. Although nonblind deconvolution performed by calibrating PSFs at different depths is the best method for recovering images, it requires complex calibrations for estimating PSFs to guarantee the accuracy. Moreover, the deblurring images obtained are time consuming. The calibration problem can be solved by allocating sufficient time for calibrations during the preparation step. However, all the prior PSFs must be used for the recovery of the images, which is unsuitable for a realistic implementation.

* Corresponding author.
E-mail address: huangw@ciomp.ac.cn (W. Huang).

https://doi.org/10.1016/j.optcom.2017.12.007
Received 9 October 2017; Received in revised form 29 November 2017; Accepted 3 December 2017
Available online 20 December 2017
0030-4018/

Fig. 1. Single-lens camera developed by authors. Effective focal length (EFL) is 35 mm, f/2.4.

Recently, Schuler proposed a nonblind deconvolution method to correct the aberrations in optical imaging systems by encoding the errors of imaging systems on a reference plane [9]. The performance of photographic single lenses was significantly improved. However, as described by Schuler, the PSF is only measured on a single calibration plane, which indicates that this method remains conventional in its nature. Further, the images used for recovery must correspond to the field of view of the reference plane; otherwise, the deblurred images will not be effectively enhanced owing to the large matching error and lack of prior PSFs. Heide suggested a robust deconvolution algorithm with a cross-channel gradient prior that enforces sparsity of hue changes across the image [10]. Although this method enhances the image quality of single-lens cameras remarkably, the shortcomings of the nonblind deconvolution methods remain. The quality of recovered images can decrease or even become unacceptable because of a defocus and object distance variance. Li designed a single-lens camera and obtained acceptable images by combining the advantages of both nonblind deconvolution methods and blind deconvolution approaches [11]. However, this method also experiences the same problems as the previous.

For image recovery, we considered other technologies that can effectively solve the shortcomings of the conventional nonblind deconvolution methods. Sparse signal representations [12–15] were considerably successful in achieving superior-image resolutions for several years. For example, many image priors can be used for learning two overcomplete dictionaries D_h and D_l, D_h for high-resolution image patches, and D_l for low-resolution patches. Each high-resolution and low-resolution image patch pair is trained to exhibit the same sparse representations. In the application, the sparse representation of a low-resolution image patch in terms of D_l can be used for determining the corresponding high-resolution image patch from D_h rapidly and accurately. Moreover, the prior PSFs can be trained to dictionaries in this manner. Therefore, it is realistic to expect that a considerable number of prior PSFs can be used for the rapid and accurate recovery of images using nonblind deconvolution methods.

Inspired by this idea, we propose a set of computational photography techniques based on sparse signal representation to correct optical aberrations. Moreover, we demonstrate the proposed methods by recovering the images obtained by a single-lens camera, as indicated in Fig. 1. Further, optical software CODE V is applied for examining the reliability of the proposed method using a simulation.

In this study, the PSF of each degraded image is first accurately calibrated using a high-quality image corresponding to the degraded image, denoted as k_k. Algorithms based on hyper-Laplacian prior [16] are used for estimating the PSF of the same scene, denoted as k_{uk}. Many PSFs of prior images are obtained using this approach. Then, PSFs k_{uk} are used for training a coupled dictionary of sparse representations. Then, the PSF of a single test image is estimated to be the same as k_{uk}, denoted as k_y. PSF k_y is sparsely represented by the coupled dictionary to obtain the most relative prior PSF k_{uk}. The PSF k_k that corresponds to the dictionary PSF k_{uk} is used for deblurring [17] the test image. Finally, a blind deconvolution method [16] is applied for reducing the algorithmic noise and matching error to acquire a sharp image. The diagram of the proposed method is displayed in Fig. 2.

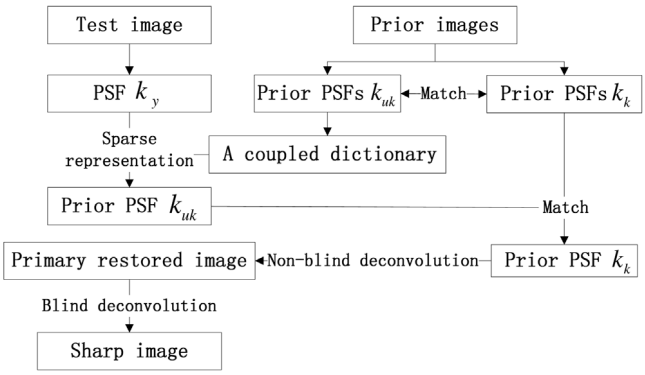

Fig. 2. Diagram of proposed method.

The remainder of this paper is organized as follows. Section 2 provides the details of the theory and method. In Section 3, the performance of the proposed method is verified using numerical tests and experiments. The conclusions are presented in Section 4. To provide a convenient and clear approach to restore the recovered images using the proposed method, we present an comprehensively detailed description of our research that includes knowledge of imaging sensors, applied optics, and digital image processing.

2. Deblurring model

In this section, we analyze the deblurring model. Image deblurring is a longstanding method that attempts to recover a sharp image from its blurred observation. The blurred image is modeled as the convolution of the sharp image with a PSF as

$$y = k \otimes x + n. \tag{1}$$

Here, y is the blurred image, x is the sharp image, k is the PSF, $\otimes$ is the 2D convolution operator, and n is the noise operator. In this study, the unknown sharp image x is recovered by $y = k \otimes x$. The overall process of the proposed approach is introduced in Algorithm 1.

Undoubtedly, degraded images can be effectively restored using prior PSFs corresponding to their own calibration planes, which is the most important advantage of nonblind deconvolution methods. For the process of recovering images, the primary idea of Algorithm 1 is to solve the problem of excessive processing time caused by the number of PSFs rather than outperform the performance of nonblind deconvolution methods. That is, the runtime of nonblind deconvolution can be significantly reduced using the proposed method when more than one prior PSF is used for restoring images. In practical applications, nonblind deconvolution methods can be suitably used for the recovery of images.

Note that every calibrated PSF has a limited depth of field because the optical aberrations vary in a nonlinear and complicated manner

Algorithm 1: Overall Process of Proposed Method

Input: blurred images, original high-quality images, and a test image

1. Prior PSFs (Section 2.1)

(1) Calculate the PSF of each blurred image with its high-quality image of the same scene using Eq. (4), denoted as k_k.

(2) Estimate the PSF of each blurred image without high-quality images using Eq. (5), denoted as k_{uk}.

The corresponding relation between k_k and k_{uk} of the same scene is established, denoted as $\{k_k, k_{uk}\}$.

2. Use prior PSFs to train a coupled dictionary (Section 2.2)

(1) Obtain the feature representation F_{uk} for k_{uk} using Eqs. (7)–(9).

(2) Train a coupled dictionary using Eqs. (14)–(16), denoted as $\{D_h, D_l\}$. Here, D_h and D_l are dictionaries of sparse representations, which are trained using prior PSFs k_{uk} and their gradient feature F_{uk}, respectively.

k_k corresponding to F_{uk} can be obtained by tracing $\{k_k, k_{uk}\}$. The corresponding relation between k_k and the elements of the coupled dictionary is denoted as $\{k_k, k_{uk}, F_{uk}\}$.

3. Image recovery (Section 2.3)

(1) Estimate the PSF of the test image without high-quality images using Eq. (5), denoted as k_y.

(2) Obtain the feature representation F_y for k_y using Eqs. (7)–(9).

(3) Predict the most relative k_{uk} using $\{D_h, D_l\}$ to sparsely represent F_y.

$Z(Eq.(17)) \rightarrow k_{Dh}(Eq.(18)) \rightarrow k_{uk}(Eq.(19)) \rightarrow k_k(\{k_k, k_{uk}, F_{uk}\})$.

(4) Use Eq. (20) to obtain the primary deblurred image u [17]. Deblur y using k_k.

(5) Further enhance the quality of image u using a blind deconvolution method [16].

Return sharp image x.

in different spaces, which makes traditional nonblind deconvolution methods unsuitable for realistic implementation. The proposed method employs numerous prior PSFs in variant planes to solve this problem. The algorithms used for obtaining the prior PSFs are described in detail in Section 2.1. In Section 2.2, the sparse representation method applied in this study is introduced. The process of image recovery is presented in Section 2.3.

2.1. Prior PSFs

We investigate prior PSFs of degraded images in Section 2.1.1. Then, the theory of depth of field is described in Section 2.1.2. This is used to demonstrate that the prior PSFs calibrated at a single depth are not sufficient for restoring images. In practice, we provide an alternative approach to determine the number of prior PSFs in the vertical direction of an object space.

2.1.1. Investigate prior PSFs

In previous studies, image alpha-matte extraction [18], gradient distribution [19], and edge feature [20] were typically used as the image prior for deconvolution methods. Although the illumination intensity for the recovery of visible images exhibits no effect on the optical aberrations, it can affect the image quality based on several factors including nonuniform illumination, environmental change, and different shooting angles. The proposed method suggests extracting the high frequencies of images as image priors to eliminate the difference caused by the variation of the illumination intensity. Discrete filters that are used for generating the high-frequency versions are represented as follows:

$$f_1 = [-1, 1], f_2 = [-1, 1]^T, \tag{2}$$

where the superscript "T" indicates a transposition. Both filters are applied for yielding two feature vectors for each image, which are concatenated into one vector as the final high-frequency versions:

$$e_{yi} = y \otimes f_i, e_{xi} = x \otimes f_i, i = 1, 2,$$

$$T_y = \{e_{y1}, e_{y2}\}, T_x = \{e_{x1}, e_{x2}\}. \tag{3}$$

In Eq. (3), T_x and T_y are the sharp image and degraded image in high-frequency space, respectively. Then, the PSFs of the degraded images are calibrated using the original high-quality images, denoted as k_k. The cost function for calculating PSF k_k is

$$\min_{k_k} \lambda \left\| T_x \otimes k_k - T_y \right\|_2^2 + \psi \left\| k_k \right\|_1. \tag{4}$$

The elements k_{ki} of k_k are subject to constraints: $k_{ki} \geq 0$, $\sum_i k_{ki} = 1$. Eq. (4) consists of two terms. The first term is applied for considering the formation model equation (1) in the high-frequency space. To reduce noise in the kernel, ℓ_1 regularization is added to k_k. The weights λ and ψ control the relative strength of k_k and the image regularization terms, respectively.

Moreover, the method in this study relies on calibrating PSFs of degraded images without high-quality images, denoted as k_{uk}. The cost function for estimating PSF k_{uk} is

$$\min_{k_{uk}} \lambda \left\| T_{uk} \otimes k_{uk} - T_y \right\|_2^2 + \frac{\left\| T_{uk} \right\|_1}{\left\| T_{uk} \right\|_2} + \psi \left\| k_{uk} \right\|_1. \tag{5}$$

Elements k_{uki} of k_{uk} are subject to the constraints that $k_{uki} \geq 0$, $\sum_i k_{uki} = 1$. Here, T_{uk} is an unknown sharp image in the high-frequency space, k_{uk} is an unknown blurring kernel. Eq. (5) comprises three terms. The operational principle of the first and the third terms are the same as those of Eq. (4). The second term is a normalized sparsity measure to encourage scale-invariant sparsity in the reconstruction [16]. Then, we can easily obtain the corresponding relation between k_k and k_{uk} using Eqs. (4) and (5), denoted as prior PSFs $\{k_k, k_{uk}\}$. The nonconvex function Eq. (5) can be optimized with an initialization on T_x and k_k, and then alternately updated between T_x and k_k. The optimization problems of Eq. (4) and (5) were solved well in [16,17].

2.1.2. Number of prior PSFs

Nonblind deconvolution methods are closely related to the depth of field of optical imaging systems. Depth of field is the distance between

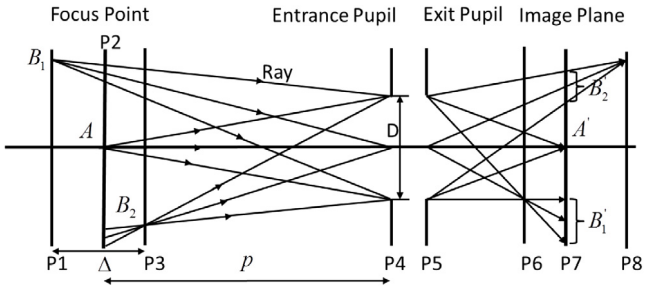

Fig. 3. Depth of field of optical imaging system.

the closest and the farthest objects in a photoappear acceptably sharp, as indicated in Fig. 3.

In Fig. 3, the depth of field Δ is the distance between $p1$ and $p3$, which can be calculated by the formula:

$$\Delta = \frac{-2pZD}{D^2 - Z^2}. \tag{6}$$

Here, A', B_1', and B_2' are the image of object A, B_1, and B_2, respectively. p is the distance between the focus point $p2$ and the entrance pupil $p4$, D is the diameter of $p4$, and Z is the minimum diameter of an object that can be distinguished by the imaging system. The smaller the Z, the higher the image quality. Theoretically, the purpose of nonblind deconvolution algorithms for imaging sensors is to reduce Z, which further corrects the optical aberrations for optical imaging systems using the prior PSFs of the calibration planes. In this case, the depth of field is denoted as Δ_c, which is obtained by combining the optical systems with prior PSFs. Further, until now, there are no nonblind algorithms that can ideally calculate optical aberrations such that the depth of field Δ_c is less than Δ when their p, Z, and D are the same. Therefore, the vertical direction of the maximal sampling interval of the calibration planes can be obtained by Eq. (6). Note that we do not consider the effect of the size of sensitization devices because the elements of the charge-coupled-device (CCD) and complementary metal-oxide semiconductor (CMOS) are frequently considerably smaller than the airy disks of simple optical systems for visible imaging.

In practice, for a simple optical system, objects are typically near its objective lens to obtain sufficient detailed texture, which indicates that Z should be small. For example, Z should be less than 0.1 mm if we want to distinguish human hairs. Therefore, according to Eq. (6), each depth of field Δ will be narrow. The relation graph of Z, p, and Δ is displayed in Fig. 4.

Fig. 4 indicates that the depth of field Δ will be greater with a decrease in entrance pupil D. According to the information in Fig. 4, Δ_c is not more than 800 mm in the worst case:. $Z = 3$ mm, $D = 23.03$ mm, and $p = 3000$ mm. If we want to distinguish objects less than 1 mm, the maximum value of Δ_c is only a few tens of millimeters. The images recovered by incorrect prior PSFs will introduce a considerable number of artifacts because of the optical aberrations that are mistakenly corrected. Therefore, in real applications, numerous prior PSFs must be used for recovering images to ensure there are suitable prior PSFs of the calibration planes that can accurately and effectively enhance the quality of the images. We further demonstrate this opinion through experiments.

2.2. Training the coupled dictionary

In this section, we extend the conventional deconvolution methods using the key idea from coupled sparse coding [21]. The prior PSFs are used for training the coupled dictionary of sparse representation. Feature transformation filters are used for extracting the characteristics of prior PSFs to ensure that the computed coefficients fit the most relevant of the coupled dictionary and enhance the prediction accuracy of the sparse representation for image reconstruction.

2.2.1. Feature representation

Typically, high-pass filters are selected for extracting the features of prior images to boost the prediction accuracy of sparse representation, such as the edge information [22], contours [23], and first and second-order gradients [24]. In this study, the first and second-order derivatives are considered as the features for PSF owing to their effectiveness and simplicity. PSF is a PSF in a matrix representation. The 1-D filters used for extracting the derivatives are as follows:

$$f_1 = [-1, 0, 1], f_3 = [1, 0, -2, 0, 1], f_2 = f_1^T, f_4 = f_3^T. \tag{7}$$

Here, T indicates transpose. Discrete filters are used for generating four feature vectors for each PSF; these are concatenated into one vector as the final representation:

$$e_{uki} = k_{uk} \otimes f_i, \tag{8}$$

$$F_{uk} = \{e_{uk1}, e_{uk2}, e_{uk3}, e_{uk4}\}. \tag{9}$$

Here, F_{uk} is a vector that includes the data of four feature vectors. Using Eqs. (7)–(9), the corresponding relation between k_{uk} and F_{uk} can be obtained, denoted as $\{k_{uk}, F_{uk}\}$. Then, the information k_k, k_{uk}, and F_{uk} of the same scene can be obtained by tracing $\{k_k, k_{uk}\}$ and $\{k_{uk}, F_{uk}\}$, denoted as $\{k_k, k_{uk}, F_{uk}\}$.

2.2.2. Training the coupled dictionary

The primary task of sparse coding is to determine a sparse representation of signals using an over-complete dictionary. In general, the dictionary is learned from a set of training examples.

In this section, our objective is to obtain the dictionaries for PSFs k_{uk} and their feature F_{uk} from sampled training pairs $\{k_{uk}, F_{uk}\}$, where $k_{uk} = \{k_{uk1}, k_{uk2}, k_{uk3}, \ldots, k_{ukn}\}$ are the set of PSFs estimated using Eq. (5) and $F_{uk} = \{F_{uk1}, F_{uk2}, F_{uk3}, \ldots, F_{ukn}\}$ are the corresponding features calculated from Eqs. (7)–(9). The sparse coding problems are

$$\min_{D_h, D_l, Z} \left\| X_c - D_c Z \right\|_2^2 + \lambda_D \left(\frac{1}{N} + \frac{1}{M}\right) \|Z\|_1, \tag{10}$$

where

$$X_c = \begin{bmatrix} \frac{1}{N} k_{uk} \\ \frac{1}{M} F_{uk} \end{bmatrix}, D_c = \begin{bmatrix} \frac{1}{N} D_h \\ \frac{1}{M} D_l \end{bmatrix}, \tag{11}$$

$$D_h = \arg\min_{D_h, Z} \left\| k_{uk} - D_h Z \right\|_2^2 + \lambda_D \|Z\|_1, \tag{12}$$

$$D_l = \arg\min_{D_l, Z} \left\| F_{uk} - D_l Z \right\|_2^2 + \lambda_D \|Z\|_1. \tag{13}$$

Here, D_h and D_l are dictionaries of sparse representations, which are trained using prior PSFs k_{uk} and their gradient feature F_{uk}, respectively. To train the coupled dictionary D_c, Eq. (10) forces PSF priors and their feature representations to share the same codes Z by combining Eqs. (11)–(13). The parameter λ_D is a weight for the sparsity regularization. N and M are the dimensions of k_{uk} and F_{uk} in the vector form, respectively. $1/N$ and $1/M$ are balance terms.

The optimization is performed in an alternative manner over Z and D_c:

(1) Select X_c using the formula:

$$\left\| X_{ci} - X_{cj} \right\|_2^2 + \lambda_D \left\| X_{ci} - X_{cj} \right\|_1 + \lambda_E \left\| X_{ci} - X_{cj} \right\|_0 \geq Q, \tag{14}$$

s.t. $i \neq j; i, j = 1, 2, \ldots, n$.

Here, Q is a threshold value used for controlling the difference between the elements of $X_c \cdot \lambda_E$ is a weight.

(2) Initialize D_c with a Gaussian random matrix with each column unit normalized.

(3) Fix D_c, update Z using the following formula:

$$Z = \arg\min_{Z} \left\| X_c - D_C Z \right\|_2^2 + \lambda_D \|Z\|_1. \tag{15}$$

(4) Fix Z, update D_c using the following formula:

$$D_c = \arg\min_{D_c} \left\| X_c - D_c Z \right\|_2^2, s.t. \left\| D_c \right\|_2^2 \leq 1. \tag{16}$$

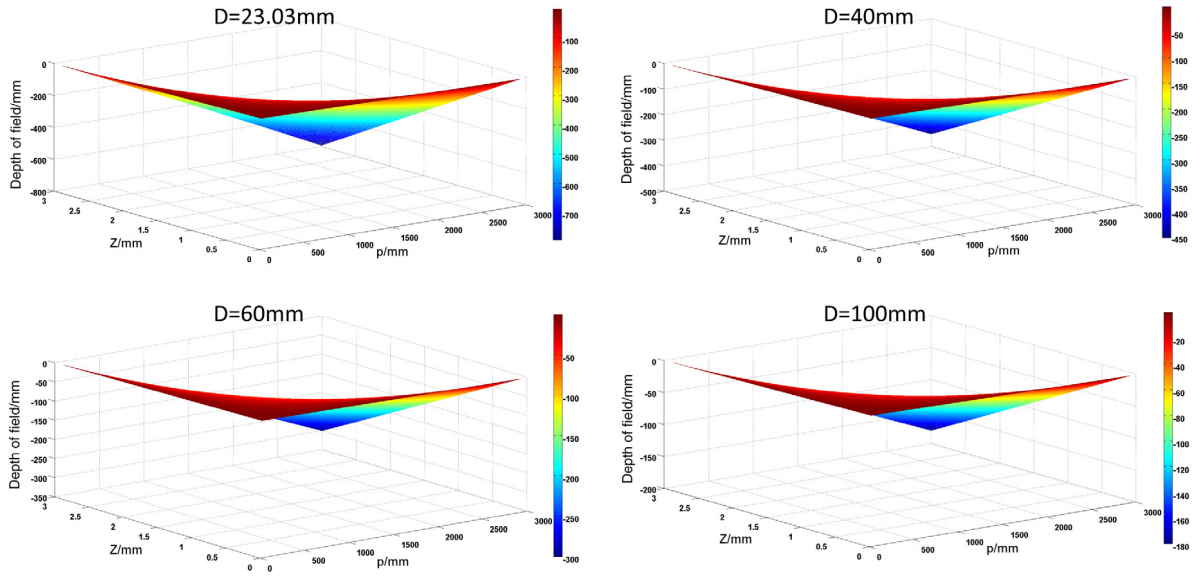

Fig. 4. Relation graph of Z, p, and Δ. Real camera in this study: $D = 23.03$ mm.

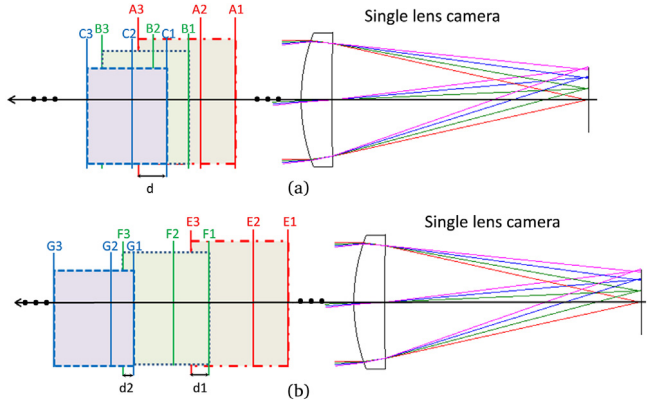

Fig. 5. Distance between *R1* and *R3* is the depth of field corresponding to calibration plane $R2, R \in \{A, B, C, E, F, G\}$. (a) Original prior PSFs; (b) prior PSFs selected by proposed method.

(5) Update $\{X_c, D_c Z\}$.

(6) Iterate between (2), (3), and (4) until convergence.

In practice, different PSFs probably recover a degraded image well if the image is obtained at the overlapping part of their depth of fields. This case should be avoided because the size of the dictionaries is limited. However, there is no discipline that can be used for selecting PSFs in different depth of fields because of the optical aberrations of imaging systems that vary in a nonlinear and complicated manner. The first step of the optimization method provides a simple and effective method to solve this problem. The unusable prior PSFs are significantly removed when the volume of data is large. The schematic is displayed in Fig. 5. Moreover, k_k, k_{uk}, F_{uk}, and $D_c Z$ of the same scene can be easily obtained by tracing the relationship $\{X_c, D_c Z\}$, denoted as $\{k_k, k_{uk}, F_{uk}, D_c Z\}$.

The prior PSFs displayed in Fig. 5 are calibrated at *A2*, *B2*, and *C2*, and denoted as *PSF1*, *PSF2*, and *PSF3*, respectively. The degraded images obtained in the overlapping part *d* can be recovered well by any one of the three prior PSFs. Moreover, all the degraded images corresponding to *PSF2* can be restored using *PSF1* and *PSF3*. A part of the volume of coupled dictionary D_c is unused by *PSF2*. Although degraded images obtained in the overlapping part *d1* and *d2* can be restored by two prior PSFs, the length between *E1* and *G3* is markedly enlarged and the unusable *PSF2* is removed. Therefore, more degraded images obtained at different depths can be recovered using suitable prior PSFs owing to the increase in the useful PSFs of the coupled dictionary.

2.3. Image recovery

In this section, Eq. (5) is used for estimating the PSF of a single test image without any high-quality images. Then, the feature of the PSF is represented by the dictionary D_l to obtain the coefficients of sparse coding. The following formula is used:

$$Z = \arg\min_{Z} \left\| F_y - D_l Z \right\|_2^2 + \lambda_D \left\| Z \right\|_1 . \tag{17}$$

Here, F_y is the feature of the PSF corresponding to the test image. Z represents the vector of the coefficients. For the model of training dictionaries, dictionaries D_h and D_l exhibit the same sparse representations for the sampled training pairs $\{k_{uk}, F_{uk}\}$. We can obtain a PSF as follows:

$$k_{Dh} = D_h Z. \tag{18}$$

Here, k_{Dh} is the PSF predicted by dictionary D_h. Typically, we cannot determine a prior PSF k_{uk} the same as k_{Dh} because the predicted PSF does not exist in the coupled dictionary. It is not realistic to train a dictionary to include all PSFs of an imaging system. As each calibrated PSF exhibits a depth of field, we proposed a method to solve this problem by predicting the most relevant k_{uk} to k_{Dh}. The function is expressed as follows:

$$k_{uk} = \arg\min_{k_{uk}} \left\| k_{uk} - D_h Z \right\|_2^2 + \delta \left\| Z \right\|_1 , k_{uk} \in \{k_k, k_{uk}, F_{uk}\}. \tag{19}$$

Here, the parameter δ balances the sparsity of the solution and the fidelity of the approximation to k_{uk}. Following this approach, the inference PSF k_k can be determined from the relationship $\{k_k, k_{uk}, F_{uk}\}$. Then, PSF k_k is used for deblurring the blurred image to obtain image u [17]:

$$\min_{u} \lambda \left\| u \otimes k_k - y \right\|_2^2 + \left\| \nabla_v y \right\|_\eta + \left\| \nabla_h y \right\|_\eta . \tag{20}$$

Here, η is a constant. Finally, the blind deconvolution algorithm of [16] is used for further enhancing the quality of image u to acquire a sharp image x.

3. Experiments

In this section, we describe the numerical experiments performed using optical software CODE V to provide prior RGB images and

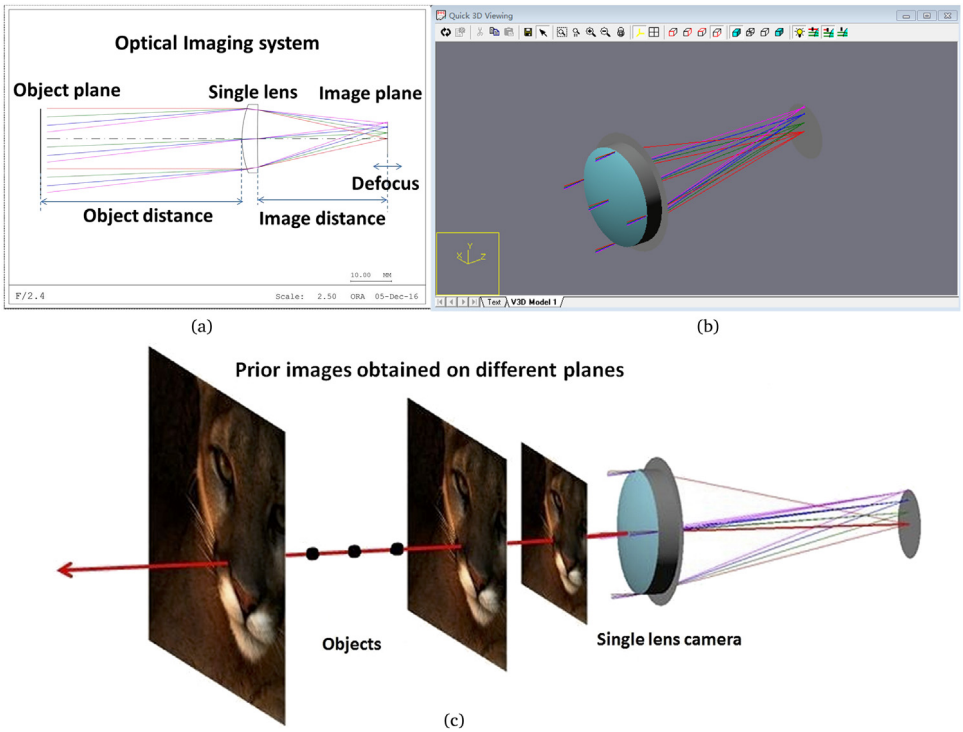

Fig. 6. (a) Sketch map of the optical imaging system; (b) 3D view of the system; (c) prior images obtained on different planes. The term "defocus" indicates that an image is obtained outside the image plane of the best focus. (For interpretation of the references to color in this figure legend, the reader is referred to the web version of this article.)

demonstrate the reliability of the proposed method. Then, we discuss whether the dictionaries provided by simulations can be used for real tests. It should be noted that CODE V is one of the most popular and reliable optical software packages used for designing optical imaging systems; it is similar to ZEMAX. The quality of images obtained using CODE V is accredited in the field of precision optics.

We do not consider algorithms that are time consuming for deblurring images in our experiments, even though they can obtain clearer images than the rapid algorithms. In addition, the field of view of the camera is not divided. Single-lens cameras with spherical surfaces typically exhibit a small field of view because their optical aberrations cannot be corrected efficiently. The images can be recovered well by PSFs of the full field of view, even though the PSFs in the center of the small field of view are different from the ones around the corners.

In practice, we observe that the upsampled version of a prior PSF is better than its original PSF for feature extraction. In this study, the original PSFs are upsampled by a factor of two using bicubic interpolation before extracting the gradient features. The parameter ψ depends on the user-specified kernel size $h(n \times n)$ according to the formula: $\psi = 3n/13$. The other parameters are $\lambda = 3000$, $\lambda_D = 0.1$, $\lambda_E = 0.01$, $\eta = 1$, $n = 19$, $Q = 1$, and $\delta = 0.1$.

Although root-mean-square error (RMSE) and structural similarity (SSIM) are common and reliable choices for image quality metrics when the reference images are provided, they are not fully reliable for evaluating the visual image quality, particularly for natural images recovered using nonblind deconvolution methods [25,26]. Prior PSFs are the most important part of nonblind deconvolution. However, it is unacceptable to calibrate different ambient brightness of a same depth of field, which leads to a significant difference between the recovered image and the original image. In the literature, it is difficult to locate studies that use the reference image assessment metric to assess visible deblurred images. In fact, currently, there is no suitable reference image assessment metric for single-lens cameras with spherical surfaces because spherical aberration, coma, astigmatism, curvature of the field, distortion, and chromatic aberration cannot be optimized well. Fortunately, no-reference image assessment metric BRISQUE [26] can effectively function for evaluating the quality of visual images.

BRISQUE operates in a special domain, which proposes a natural scene statistic-based distortion-generic blind/no-reference image-quality assessment model. The scene statistics of locally normalized luminance coefficients are used for holistically measuring the quality of the visual images, which quantifies the possible losses of "naturalness" instead of computing the distortion-specific features such as blocking and ringing. Further, a previous study [26] demonstrated that BRISQUE is statistically superior to the full-reference structural similarity index and is highly competitive with respect to all present-day distortion-generic, no-reference image-quality assessment algorithms.

BRISQUE is applied for rating the blurred and recovered images to quantify the performance of the proposed method. The score typically exhibits a value between zero and 100 (zero represents the best quality, 100 the worst). The smaller the value of BRISQUE, the higher the image quality. We also provide the value obtained using RMSE and SSIM [27].

All simulations were conducted on a 4.0 GHz Intel Core-i7 6700 K workstation with 32 GB RAM and Ubuntu 14.04 operating system. The algorithms were compiled by MATLAB R2011b.

3.1. Numerical experiments

3.1.1. Prior images

The simulation model used for obtaining prior images is displayed in Fig. 6. The shape of the field of view of a single-lens camera is circular. Moreover, the target size is the same as the size of the largest square within the circular area. In practice, optical defocus must be considered because the majority of the images obtained by cameras are outside the scene plane. The object distance was selected from 100 mm to 6000 mm with a sample interval of 10 mm to obtain sufficient experimental data. The range of the defocus value was from 0 mm to 60 mm with an interval of 1 mm. The number of prior images was approximately 36,000. Notice that there is no limitation on the number of prior images used for the experiments when the useful prior PSFs cover the region of interest. Further, a problem that should be noted is that the smaller the sampling interval, the higher the accuracy of prediction. We further describe this

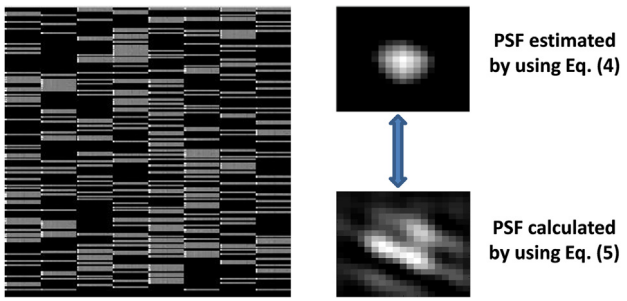

Fig. 7. (a) Dictionary D_h, D_l — 1024 dictionary atoms are learned with each atom size equal to 19; (b) PSFs of the same image are obtained by Eqs. (4) and (5), respectively. The PSFs calculated using Eq. (5) are applied for training the coupled dictionary. The PSFs estimated by Eq. (4) are used for recovering images.

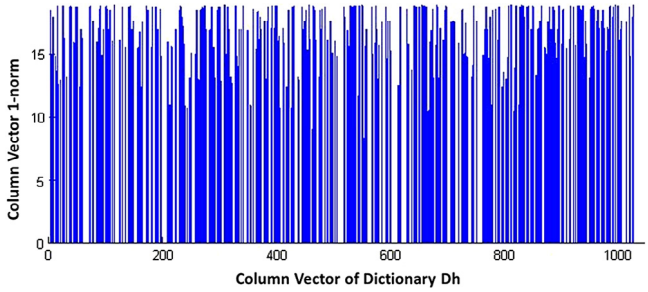

Fig. 8. Experimental example: the real dictionary size 380 is smaller than the target value 1024. The blank positions along the horizontal axis are invalid data.

in a later section. In the previous case, more prior PSFs will be required for training dictionaries if the area of interest is enlarged.

The single-lens camera displayed in Fig. 6 corresponds to the camera displayed in Fig. 1. The wavelength of the red line, forest green line, and blue line is 656.27250 nm, 587.56180 nm, and 486.13270 nm, respectively.

3.1.2. Coupled dictionary

The coupled dictionary was trained using 36,000 PSF pairs sampled from the prior images as indicated in Fig. 7. The maximum size of the dictionaries was determined by the threshold value Q and number of prior PSFs. The value of Q was applied to preliminarily control the difference between the elements of the dictionaries, as previously described. It can be set to zero if prior PSFs are insufficient. The maximum number of elements of each dictionary should not exceed the number of prior PSFs; otherwise, the dictionaries will become invalid.

Importantly, the threshold value of Eq. (14) and the iteration accuracy of Eqs. (15) and (16) must be carefully selected. The real size of the trained dictionary will be smaller than the target value if the threshold and iteration accuracy are selected incorrectly, as indicated in Fig. 8. The simulation result for a dictionary is used for explaining this statement, where the real size 380 is smaller than the expected size 1024. In this case, we could use a smaller dictionary for the proposed method if its atoms have covered the area of interest.

3.1.3. Simulation results

3.1.3.1. Recover images using proposed method at different depths. In this subsection, many experiments were performed for evaluating the performance of the proposed method. The images obtained at different depths were restored using the proposed method, as displayed in Fig. 9. Each test image was recovered by two PSFs. One was the prior PSF calibrated using an original high-quality image of the same scene, which was used for the recovery of primary images. The other was the PSF provided by the blind deconvolution method [16], which was applied to remove the effect of algorithm noise and matching error. The RMSE, SSIM, and BRISQUE test results are listed in Table 1.

Table 1
RMSE, SSIM, and BRISQUE test results.

Image	Original	Blur	Recovery
Building			
RMSE		30.6157(a1)	34.0414(a4)
		33.8568(a2)	37.3102(a5)
		35.8223(a3)	37.6692(a6)
SSIM		0.21560(a1)	0.21660(a4)
		0.16730(a2)	0.13710(a5)
		0.14530(a3)	0.11820(a6)
BRISQUE	19.6802(a)	52.1378(a1)	**36.2165(a4)**
		59.4542(a2)	**32.9700(a5)**
		65.4440(a3)	**39.6778(a6)**
Bear			
RMSE		16.6205(d1)	15.5276(d4)
		17.9957(d2)	16.7491(d5)
		18.5261(d3)	18.6848(d6)
SSIM		0.49860(d1)	0.53030(d4)
		0.47890(d2)	0.49470(d5)
		0.47240(d3)	0.42280(d6)
BRISQUE	17.6020(d)	67.0404(d1)	**48.0821(d4)**
		73.5847(d2)	**37.9411(d5)**
		73.7535(d3)	**46.3678(d6)**

Fig. 9 indicates that the images obtained at different depths can be significantly enhanced by the proposed method using different prior PSFs. In these results, the minimum BRISQUE value of the test images was approximately 52, which indicates that the texture of the images was difficult to identify. Although the single-lens camera suffers from heavy aberrations, the texture of the restored images can be observed more clearly. The experimental results demonstrate that the proposed method can significantly enhance the quality of images.

Further, the Table 1 results indicate that RMSE and SSIM are inadequate to evaluate the quality of recovered images because all the images restored are certainly enhanced. BRISQUE can effectively provide details regarding the quality of images according to subjective sensation and objective evaluation.

3.1.3.2. Recover images of the same scene using different methods. Experimental results obtained using different methods are compared on the same plane, as displayed in Fig. 10. The RMSE, SSIM, and BRISQUE test results are listed in Table 2.

The images recovered using blind deconvolution method [16] are noticeably smooth and lack detailed texture. Their reduced quality is particularly visible at the profile of the magnified part, which is noticeably jagged. According to the BRISQUE values, the images restored using the nonblind deconvolution approach [17] exhibited superior quality. However, the detailed texture cannot be observed clearly. Both the subjective feeling and objective evaluation demonstrate that the proposed method outperformed the others.

3.1.3.3. Recover images of different depths using several methods. Every calibrated PSF exhibits a limited depth of field because the optical aberrations vary in a nonlinear and complicated manner in different spaces. Although nonblind deconvolution algorithms can remarkably enhance the quality of images, the prior PSFs are typically measured at a single depth, which leads to inadequate results or even failures when the objects are outside the depth of field of the calibration plane. This problem of nonblind deconvolution methods can be easily solved using the proposed method. Compared with the methods provided by Schuler [9] and Heide [10], the operating time cost by Li [11] was the shortest and with practical application values. For a better comparison, the results of nonblind deconvolution algorithms [17], Li [11], and the proposed method are displayed in Fig. 11. The RMSE, SSIM, and BRISQUE test results are listed in Table 3.

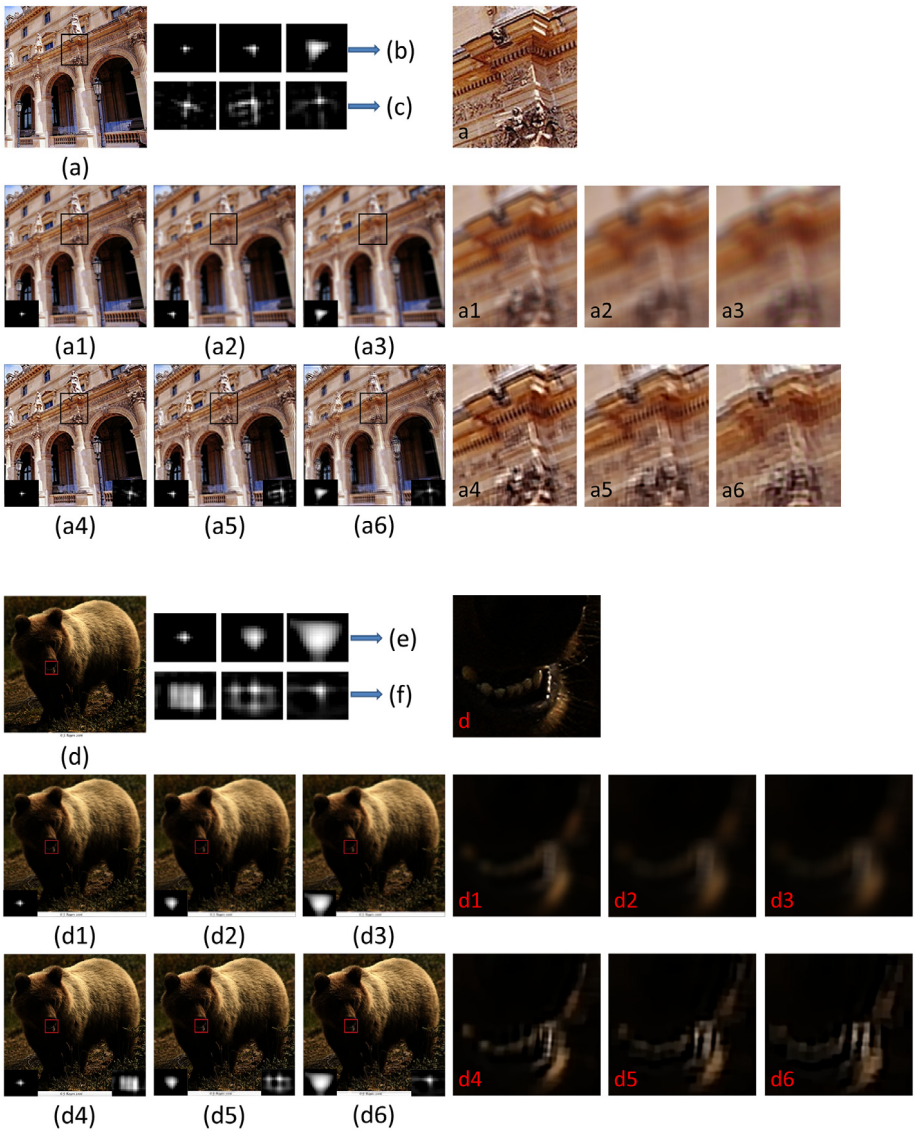

Fig. 9. (a) and (d) Original image of a building and a bear, respectively; (a1), (a2), (a3), (d1), (d2), and (d3) blurred images and their blurred kernels obtained using Eq. (4); (a4), (a5), (a6), (d4), (d5), and (d6) images deblurred by proposed method. Each deblurred image was directly under the respective blurred image; (b) and (e) PSFs obtained using Eq. (4); (c) and (f) PSFs calculated using Eq. (5). In each image, the inset in the corner corresponds to the magnified image on the right.

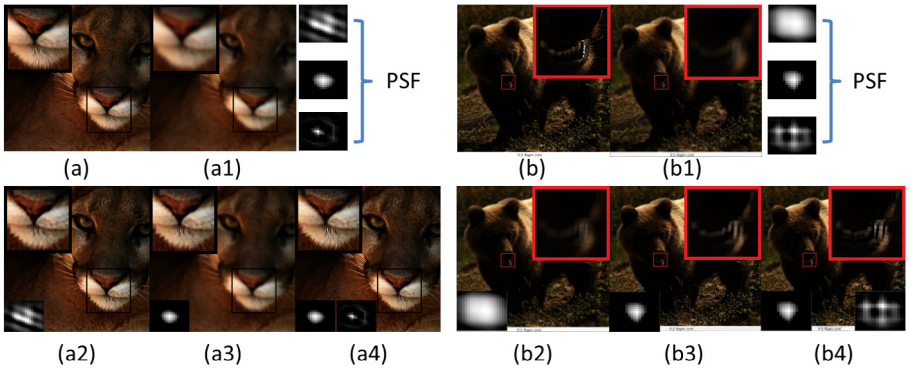

Fig. 10. (a) and (b) Original image of a lion and a bear, respectively; (a1) and (b1) blurred images; (a2) and (b2) images restored by blind deconvolution method [16]; (a3) and (b3) images deblurred by nonblind deconvolution method [17]; (a4) and (b4) images recovered by proposed method. In each image, the inset corresponds to the black rectangle.

In this section, for the images of the lion, the second and third blurred images were obtained near the reference plane that corresponds to the first image. To demonstrate that every calibrated PSF exhibits a limited depth of field and one prior PSF used to recover images is not sufficient, only the first and second images were covered by the depth of field of the prior PSF using the method of [11]. The experiments with the

Table 2
RMSE, SSIM, and BRISQUE test results.

Method	Original	Blur	Blind [16]	Non-blind [17]	Proposed
Lion					
RMSE		6.7562(a1)	6.7564(a2)	6.0860(a3)	8.1847(a4)
SSIM		0.6983(a1)	0.6411(a2)	0.7102(a3)	0.5889(a4)
BRISQUE	17.8475(a)	52.6462(a1)	35.9561(a2)	26.6553(a3)	**25.9909(a4)**
Bear					
RMSE		17.9957(b1)	15.5122(b2)	18.1587(b3)	16.7491(b4)
SSIM		0.4789(b1)	0.4988(b2)	0.4734(b3)	0.4947(b4)
BRISQUE	17.6020(b)	73.5847(b1)	60.0156(b2)	53.0156(b3)	**37.9411(b4)**

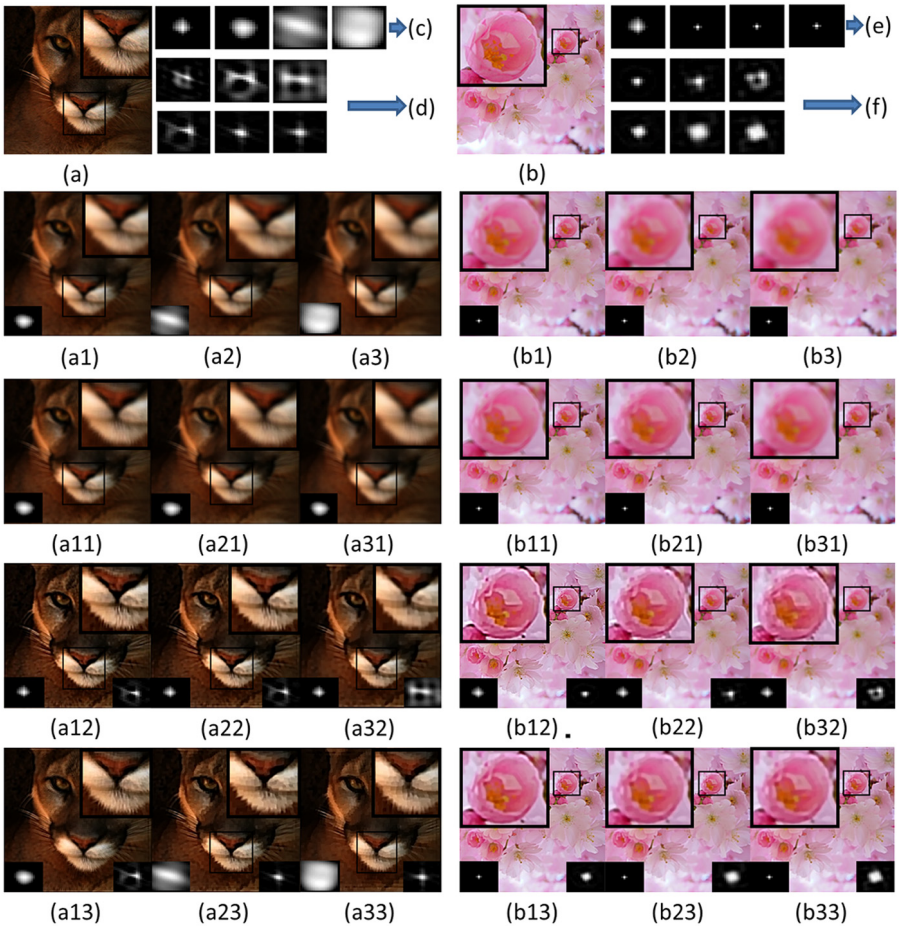

Fig. 11. (a) and (b) Original images of a lion and flowers, respectively; (a1), (a2), (a3), (b1), (b2), and (b3) blurred images and their blurred PSFs; (a11), (a21), and (a31) images recovered with the calibrated prior PSF of image (a11); (b11), (b21), and (b31) images recovered with the calibrated prior PSF of image (b11); (a12), (a22), (a32), (b12), (b22), and (b32) images recovered using the method of Li [11]. The prior PSF was calibrated at the depth of 600 mm (object distance); (a13), (a23), (a33), (b13), (b23), and (b33) images recovered using proposed method; (c) and (e) Blurred PSFs estimated using Eq. (4) are used to recover images; (d) and (f) PSFs calculated by the blind deconvolution method [16] are applied to further enhance the quality of the test images. In each image, the inset corresponds to the rectangle.

images of flowers were used to further demonstrate that different depth of fields can remarkably affect the quality of deblurred images, although the difference of the calibrated PSFs is considerably small.

For the images of the lion, the simulation results reveal that the nonblind deconvolution method [17] leads to a lower quality recovery for the second blurred image and to an apparent recovery failure for the third. Although, the first and second images are visibly enhanced using Li [11], the third image was unsuccessfully restored. For the images of flowers, only the first image recovered by the nonblind deconvolution method [17] is enhanced. The images recovered by Li [11] and the proposed method are certainly enhanced.

However, all the images recovered by Li [11] exhibit considerable visual artifacts because of the lack of proper prior PSFs. The images deblurred by the proposed method indicate considerable enhancement, particularly for the subjective feeling because the proposed method can recover images using suitable and accurate prior PSFs corresponding to their calibration planes.

3.1.3.4. Runtime. Although nonblind deconvolution methods are the best methods for recovering images, their time requirement is unacceptable. This problem can be easily solved by combining them with the proposed method, which moves this problem to the preparation step. Therefore, nonblind deconvolution methods can be effectively used for recovering images. The runtimes for the proposed method and others obtained in the same computing environment are listed in Table 4. The number of calibrated PSFs was 1024 in all cases.

It requires 1024 runs for the image processing using the nonblind deconvolution method to obtain images recovered by all the PSFs, which makes it impractical in realistic applications. Although all the prior PSFs are used by the proposed method, the running time is significantly less

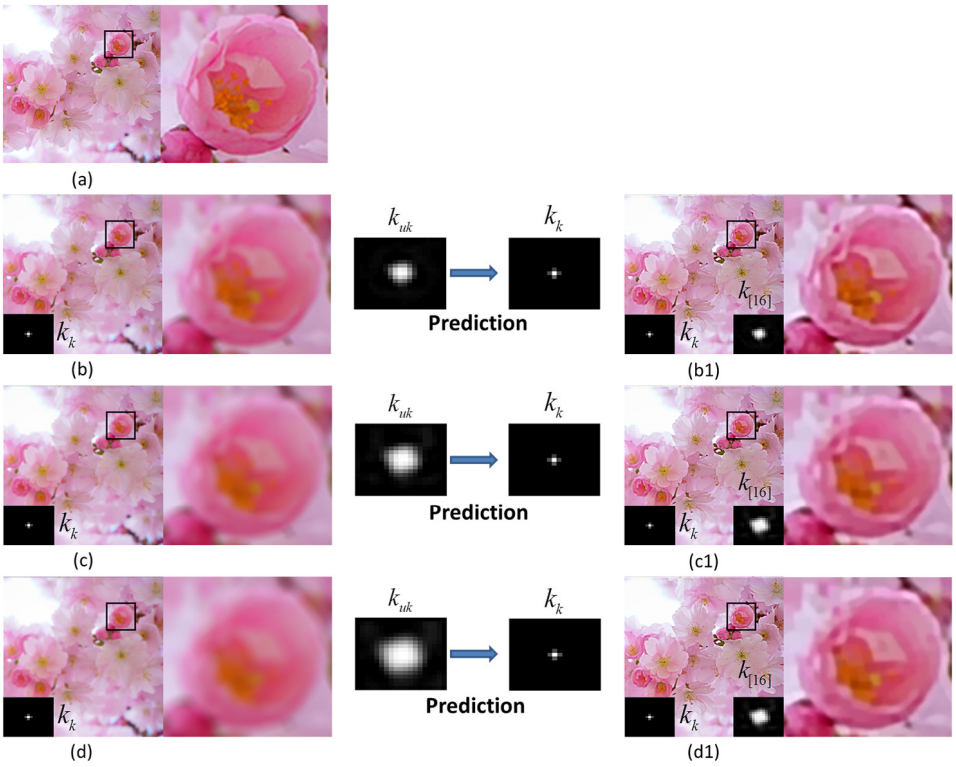

Fig. 12. (a) Original image; (b), (c), and (d) blurred images and their blurred kernels obtained using Eq. (5); (b1), (c1), and (d1) deblurred with proposed method. PSFs $k_{[16]}$ calculated using Eq. (6) were applied to eliminate the influence of the algorithm noise and matching error.

Table 3
RMSE, SSIM, and BRISQUE test results.

Method	Original	Blur	Non-blind [17]	Li [11]	Proposed
Lion					
RMSE		7.96030(a1)	8.41000(a11)	9.04730(a12)	9.56840(a13)
		8.29660(a2)	8.59610(a21)	9.04620(a22)	10.6684(a23)
		9.14700(a3)	9.14440(a31)	9.90140(a32)	8.28470(a33)
SSIM		0.59950(a1)	0.57210(a11)	0.62530(a12)	0.55730(a13)
		0.58910(a2)	0.60080(a21)	0.60710(a22)	0.51510(a23)
		0.57110(a3)	0.60650(a31)	0.56300(a32)	0.55580(a33)
BRISQUE	19.7489(a)	65.0576(a1)	43.7874(a11)	44.9771(a12)	**44.5731(a13)**
		66.6472(a2)	50.8924(a21)	50.2016(a22)	**47.9862(a23)**
		70.7585(a3)	58.7096(a31)	61.7998(a32)	**49.6250(a33)**
Flowers					
RMSE		9.47470(b1)	10.0534(b11)	13.5670(b12)	12.8915(b13)
		11.4273(b2)	11.7468(b21)	14.5177(b22)	15.2672(b23)
		12.5117(b3)	11.7468(b31)	14.7770(b32)	15.2683(b33)
SSIM		0.86660(b1)	0.86760(b11)	0.89480(b12)	0.87120(b13)
		0.82250(b2)	0.82250(b21)	0.83310(b22)	0.84390(b23)
		0.79430(b3)	0.82230(b31)	0.79590(b32)	0.84390(b33)
BRISQUE	34.2611(b)	56.5977(b1)	54.9123(b11)	27.0388(b12)	**31.5485(b13)**
		66.8050(b2)	66.4969(b21)	30.0944(b22)	**38.1314(b23)**
		71.4165(b3)	67.3193(b31)	39.0598(b32)	**39.0254(b33)**

than that of method [17]: 20471.10 s are decreased to 38.85 s. The results reveal that the proposed method is rapid and the processing speed is acceptable, even though the runtime is twice that of the blind deconvolution method.

3.1.3.5. Analyze prediction. Not only can the nonblind deconvolution methods use many prior PSFs by employing the proposed method but they can also considerably match the precision. The prior PSFs used for recovering images were predicted using PSFs k_{uk} rather than PSFs k_k. Therefore, the prediction accuracy rapidly increased. To demonstrate this statement, images obtained in the same depth of field are displayed in Fig. 12. The RMSE, SSIM, and BRISQUE test results are listed in Table 5.

Table 4
Runtimes (s).

Method	Blind [16]	Non-blind [17]	Li [11]	proposed
Building	19.76	20471.10	39.12	**38.85**
Lion	21.13	23747.59	40.95	**41.20**
Bear	22.78	24308.64	41.13	**42.33**

Fig. 12 indicates that the prior PSFs k_k corresponding to the images can be accurately predicted using PSFs k_{uk}, their difference is small. For a detail comparison, PSFs of the first image (b) are the reference. The differential chart is displayed in Fig. 13. In this case, Fig. 13 indicates that PSFs k_{uk} are easier to be distinguished than PSFs k_k.

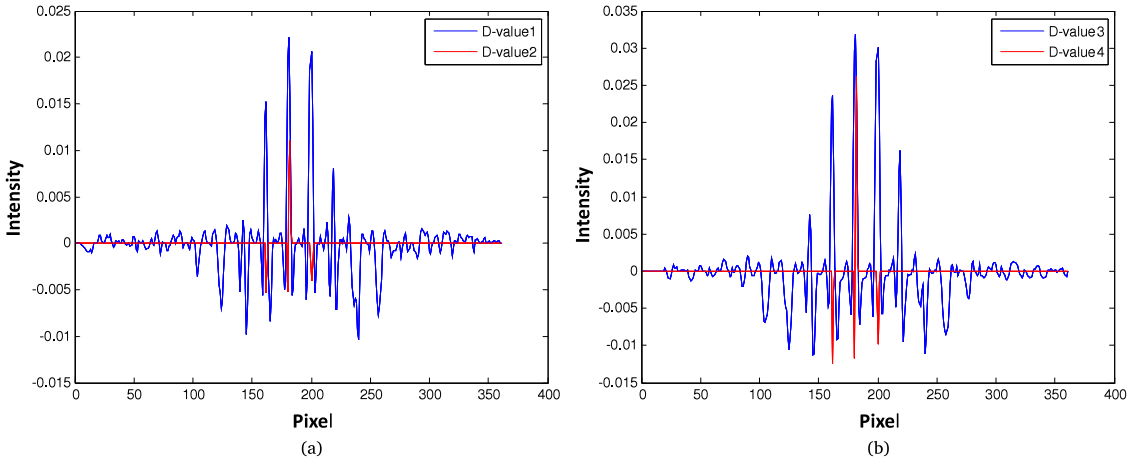

Fig. 13. (a) D-value1: Difference of PSFs k_{uk} corresponding to images (b) and (c) displayed in Fig. 10. D-value2: Difference of PSFs k_k corresponding to images (b) and (c) displayed in Fig. 10; (b) D-value3: Difference of PSFs k_{uk} corresponding to images (b) and (d) displayed in Fig. 10. D-value4: Difference of PSFs k_k corresponding to images (b) and (d) displayed in Fig. 12.

Fig. 14. Hardware setup employed to perform the test. Number of recording pixels: 1920 (H) × 1080 (V) approx. 2.07 M. Unit cell size: 3.75 μm (H) × 3.75 μm (V).

Table 5
RMSE, SSIM, and BRISQUE test results.

Image	Original	Blur	Recovery
RMSE		9.47470(b)	12.8915(b1)
		11.4273(c)	15.2672(c1)
		12.5117(d)	15.2683(d1)
SSIM		0.86660(b)	0.87120(b1)
		0.82250(c)	0.84390(c1)
		0.79430(d)	0.84390(d1)
BRISQUE	34.0681(a)	56.5977(b)	**35.5485(b1)**
		66.8050(c)	**38.1314(c1)**
		71.4165(d)	**39.0254(d1)**

3.2. Real camera test results

Clearly, nonblind deconvolution methods are no longer limited by the number of prior PSFs in the proposed method. However, we require considerable time to calibrate sufficient PSFs to guarantee the accuracy. For single-lens cameras, an alternative approach to conveniently obtain valid prior PSFs is provided and demonstrated in this section.

Fig. 14 displays the experimental setup including a CMOS (IMX185LQ-C) camera and a laptop with a VideoLAN Client (VLC) media player. The camera uses a diagonal 8.58 mm (Type 1/1.9) CMOS active pixel-type solid-state image sensor with a square pixel array and 2.38 M effective pixels. The real single-lens camera corresponds to the simulation model.

In the real application, the difference between the single lens designed by CODE V and the real lens is minimal. Line spread functions of the real camera and the simulation model are used for demonstrating this statement. The line spread functions measured by the line spread function measuring equipment and CODE V are displayed in Fig. 15, which includes the radial and tangential Line Spread Function (LSF). However, there is no reference image assessment metric for the LSF of optical lenses. In practice, we can be satisfied if the variation trend of the real lens is the same as the designed lens. The results reveal that the LSFs of the single-lens camera are in accord with the designed LSFs. Therefore, we can attempt to restore real images using the information obtained from the simulation model.

Previous studies indicate the fact that blind deconvolution methods are seldom used for restoring the images of imaging systems suffered from heavy aberrations. Nonblind deconvolution methods can effectively enhance the quality of blurred images owing to the use of accurate solutions to reversely obtain sharp images. The primary purpose of the proposed method is to solve the problem of excessive processing time caused by the number of PSFs rather than outperform the performance of nonblind deconvolution methods, as indicated in Table 4. Evidently, the operating time of nonblind deconvolution methods can be reduced significantly using the proposed method when more than one prior PSF is used for restoring the images. Still, for single-lens cameras, the proposed method is the first one that makes nonblind deconvolution methods suitable for realistic implementations. To demonstrate that the prior information obtained by CODE V can also be used for addressing real images of single-lens cameras, the performance of the proposed method was compared with that of the method of Li [11].

In a real application, it is difficult to obtain a clear image of a small target using single-lens cameras owing to heavy aberrations. Typical results are displayed in Fig. 16. The object distance of the real tests is arbitrarily selected near 600 mm. The first and second objects are obtained at the same object distance. The length and width of the first and second objects are as follows: 80 mm × 65 mm and 30 mm × 20 mm. The prior PSF of the method of Li [11] is accurately calibrated at a depth of 600 mm, which corresponds to the same distance of the simulation experiment. The BRISQUE test results are listed in Table 6.

The quality of the images recovered using the method of Li [11] is less than the quality of images recovered using the proposed method; the quality of images is even less than image (c1) recovered using the method of [16]. This demonstrates that prior PSFs calibrated at a single depth are insufficient for image recovering. The results of the proposed method reveal that the quality of the images is remarkably enhanced. Both the subjective feeling and the objective evaluation demonstrate that the prior PSFs provided by CODE V can be used for the

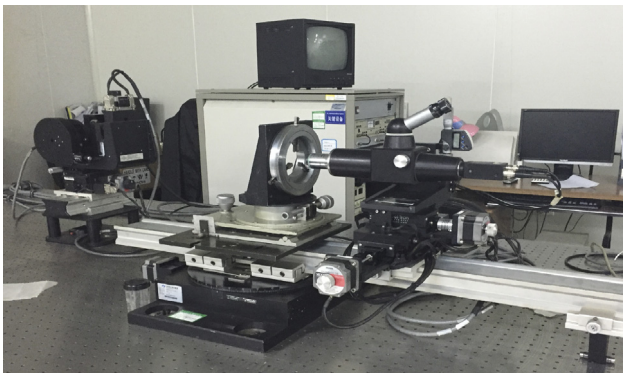

(a) Line spread function measuring equipment.

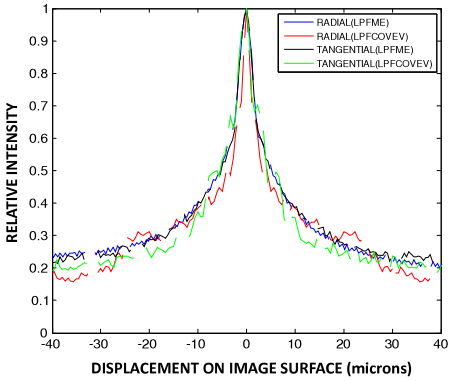

(b) Line spread functions.

Fig. 15. (a) Line spread function measuring equipment; (b) line spread functions of the radial and tangential measured by line spread function measuring equipment and CODE V. Line spread function measuring equipment (LPFME). Line spread function CODE V (LPFCOEV).

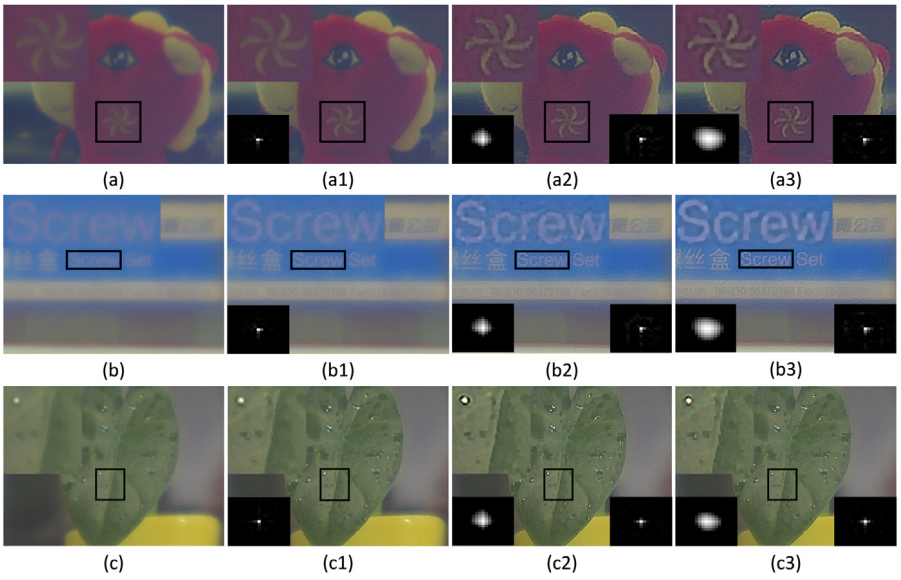

Fig. 16. (a)–(c) Blurred images; (a1)–(c1) image restored by blind deconvolution method [16]; (a2)–(c2) image restored by Li [11]; (a3)–(c3) images restored by proposed method.

Table 6
BRISQUE test results.

Method	Blur	Recovery
[16]	47.3460(a)	46.5053(a1)
	52.4438(b)	45.1133(b1)
	42.5599(c)	30.5672(c1)
Li [11]	47.3460(a)	41.6049(a2)
	52.4438(b)	42.1358(b2)
	42.5599(c)	34.0324(c2)
Proposed	47.3460(a)	39.5236(a3)
	52.4438(b)	39.6658(b3)
	42.5599(c)	28.9692(c3)

implementation of a realistic single-lens camera, thereby providing an alternative approach to conveniently obtain valid PSFs of a single-lens camera.

4. Conclusion

The primary objective of our study was to provide an alternative method for capturing high-quality photographs for single-lens cameras, which is suitable for a realistic implementation. This paper presented an approach of image deblurring based on sparse representations in terms of coupled dictionaries jointly trained from PSF pairs, which clearly enhanced the quality of the images obtained using a single-lens camera.

In more detail, both the numerical and experimental results demonstrated the effectiveness of the sparsity prior for recovering images. In particular, the blurred images of the single-lens camera were effectively restored using prior PSFs obtained by simulations, thus suggesting a valid and convenient approach to obtain the PSFs of single-lens cameras. Moreover, the concept of sparse representations can be generally used in deconvolution methods and optical imaging systems for further enhancing the quality of recovered images.

In real application, the prior PSF and space position corresponding to any imaging object can be accurately found. Then, the imaging quality of the imperfect optical system can be improved by using non-blind deconvolution methods. In addition, the proposed method is particularly important for non-blind deconvolution methods, because it offers a solution for challenges such as excessive processing time and field of view problems, which indicates that these methods will no longer be restricted by the number of prior PSFs. The PSF size can affect the quality of a recovered image because of several factors such as the field of view of the optical imaging systems, size of the images, and quality of the blurred images. We are investigating this problem in terms of the characteristic analysis of the PSFs and automatic seamless image mosaic based on feature points.

Acknowledgments

The authors gratefully acknowledge the support by the State Key Laboratory of Applied Optics, Changchun Institute of Optics, Fine Mechanics and Physics, Chinese Academy of Sciences [grant number Y4223FQ147].

References

[1] R. Raskar, J. Tumblin, A. Mohan, Computational photography, Eurographics (STARs) 1 (1) (2006) 1–20.
[2] W. Dong, H. Feng, Z. Xu, Multi-frame blind deconvolution using sparse priors, Opt. Commun. 285 (9) (2012) 2276–2288.
[3] T. Yue, J. Suo, J. Wang, Blind optical aberration correction by exploring geometric and visual priors, in: Proceedings of the IEEE Conference on Computer Vision and Pattern Recognition, 2015, pp. 1684–1692.
[4] D. Shi, C. Fan, H. Shen, Application of multi-frame approach in single-frame blind deconvolution, Opt. Commun. 285 (24) (2012) 4937–4940.
[5] E. Vera, M. Vega, R. Molina, Iterative image restoration using nonstationary priors, Appl. Opt. 52 (10) (2013) D102–D110.
[6] T.J. Holmes, Y.H. Liu, Richardson-Lucy/maximum likelihood image restoration algorithm for fluorescence microscopy: Further testing, Appl. Opt. 28 (22) (1989) 4930–4938.
[7] C.J. Schuler, Burger,H. Christopher, S. Harmeling, A machine learning approach for non-blind image deconvolution, in: Proceedings of the IEEE Conference on Computer Vision and Pattern Recognition, 2013, pp. 1067–1074.
[8] L. Yuan, J. Sun, L. Quan, Progressive inter-scale and intra-scale non-blind image deconvolution, ACM Trans. Graph. 27 (3) (2008) 74.
[9] C.J. Schuler, M. Hirsch, S. Harmeling, Non-stationary correction of optical aberrations, in: 2011 IEEE International Conference on Computer Vision (ICCV), IEEE, 2011, pp. 659–666.
[10] F. Heide, M. Rouf, M.B. Hullin, High-quality computational imaging through simple lenses, ACM Trans. Graph. 32 (5) (2013) 149.
[11] W. Li, Y. Liu, X. Yin, A computational photography algorithm for quality enhancement of single lens imaging deblurring, Optik 126 (21) (2015) 2788–2792.
[12] L. He, H. Qi, R. Zaretzki, Beta process joint dictionary learning for coupled feature spaces with application to single image super-resolution, in: Proceedings of the IEEE Conference on Computer Vision and Pattern Recognition, 2013, pp. 345–352.
[13] H. Zhang, Y. Zhang, T.S. Huang, Efficient sparse representation based image super resolution via dual dictionary learning, in: 2011 IEEE International Conference on Multimedia and Expo (ICME), IEEE, 2011, pp. 1–6.
[14] K. Zhang, X. Gao, D. Tao, Multi-scale dictionary for single image super-resolution, in: 2012 IEEE Conference on Computer Vision and Pattern Recognition (CVPR), IEEE, 2012, pp. 1114–1121.
[15] H. Liu, S. Li, H. Yin, Infrared surveillance image super resolution via group sparse representation, Opt. Commun. 289 (2013) 45–52.
[16] D. Krishnan, T. Tay, R. Fergus, Blind deconvolution using a normalized sparsity measure, in: 2011 IEEE Conference on Computer Vision and Pattern Recognition (CVPR), IEEE, 2011, pp. 233–240.
[17] D. Krishnan, R. Fergus, Fast image deconvolution using hyper-Laplacian priors, Adv. Neural Inf. Process. Syst. (2009) 1033–1041.
[18] J. Jia, Single image motion deblurring using transparency, in: IEEE Conference on Computer Vision and Pattern Recognition, 2007, CVPR'07, IEEE, 2007, pp. 1–8.
[19] R. Fergus, B. Singh, A. Hertzmann, Removing camera shake from a single photograph, ACM Trans. Graph. 25 (3) (2006) 787–794.
[20] N. Joshi, R. Szeliski, D.J. Kriegman, PSF estimation using sharp edge prediction, in: IEEE Conference on Computer Vision and Pattern Recognition, 2008, 2008 CVPR, IEEE, 2008, pp. 1–8.
[21] J. Yang, Z. Wang, Z. Lin, Coupled dictionary training for image super-resolution, IEEE Trans. Image Process. 21 (8) (2012) 3467–3478.
[22] W.T. Freeman, E.C. Pasztor, O.T. Carmichael, Learning low-level vision, Int. J. Comput. Vis. 40 (1) (2000) 25–47.
[23] J. Sun, N.N. Zheng, H. Tao, Image hallucination with primal sketch priors, in: 2003 IEEE Computer Society Conference on Computer Vision and Pattern Recognition, 2003. Proceedings, Vol. 2, IEEE, 2003, II–729.
[24] H. Chang, D.Y. Yeung, Y. Xiong, Super-resolution through neighbor embedding, in: Proceedings of the 2004 IEEE Computer Society Conference on Computer Vision and Pattern Recognition, 2004. Vol. 1, CVPR 2004, IEEE, 2004, I–I.
[25] Z. Wang, A.C. Bovik, Mean squared error: love it or leave it? A new look at signal fidelity measures, IEEE Signal Process. Mag. 26 (1) (2009) 98–117.
[26] A. Mittal, A.K. Moorthy, A.C. Bovik, No-reference image quality assessment in the spatial domain, IEEE Trans. Image Process. 21 (12) (2012) 4695–4708.
[27] Z. Wang, E.P. Simoncelli, A.C. Bovik, Multiscale structural similarity for image quality assessment, in: Conference Record of the Thirty-Seventh Asilomar Conference on Signals, Systems and Computers, 2004, Vol. 2, IEEE, 2003, pp. 1398–1402.